

## **Multiparameter inverse scattering: computational approaches**

Glen R. Young, Kris Innanen and Laurence R. Lines

### **ABSTRACT**

The use of inverse scattering methods in the inversion of seismic data has been on the rise in exploration geophysics. With specific computational approaches it is possible to ascertain the material properties of the subsurface using scattered acoustic waves. We seek to determine multiple rock parameters such as density and bulk modulus from reflected seismic signals. At this early stage of investigation a basic approach is used based on straightforward inverse scattering equations. In this case we will examine how multiparameter inverse scattering in a constant 2D background works and what are the results of inverting synthetically generated data. A simulation was developed for this project in two parts. The forward modeling stage and the inversion. The forward modeling code is based upon CREWES MATLAB finite difference routines, this stage takes simple user generated velocity models and shot patterns and creates a set of synthetic shot profiles which are convolved with a Ricker source wavelet. The second stage takes these shot profiles and attempts a deconvolution and inversion to generate an inversion image. The inversion image is then examined for accuracy and various models are used to determine if physically realistic effects are present as would be seen in real seismic data.

### **INTRODUCTION**

In the field of exploration geophysics, the inversion of seismic data obtained from expensive seismic survey operations is of paramount importance to various resource based industries. Specifically in the interpretation and location of petroleum bearing subsurface formations as well as in general subsurface mapping of other geologic structures for economic and scientific purposes.

The knowledge of the physical parameters of subsurface structures is vitally important in the exploration process, these telltale indicators are the guide to which many other decisions in the economic exploitation chain are made. The proper interpretation of these indicators yields successful recovery operations, the failure to gain accurate data for these interpretations can lead to unwanted and wasteful expenditures of time and money.

Inversion methods have been around since the beginning of exploration geophysics but many algorithms and methods developed in the past have been limited by the computational resources available at the time. Many are still being developed today which can fully exploit the use of modern computer technology and thus are becoming the standard instruments in the repertoire of essential tools in exploration geophysics. Other methods which were detailed in the past were more in the class of intellectual curiosities due to the limited computational power and lack of efficiency of the facilities available at the time and were thus forgotten by modern researchers after their publication, some only now being rediscovered and investigated further.

In this investigation we will perform numerical experiments to determine the properties and locations of subsurface structures and their physical parameters using inverse scattering

methods. The primary method is based on the paper by Clayton and Stolt (1981), published when desktop computing power was  $10^{-6}$  that of today's typical machines. This paper details the algorithms required to properly image and obtain an inversion of seismic data for two cases, the constant background and the variable background. In our case we will attempt to examine only the constant background case and only in a 2 dimensional(2D) seismic geometry.

Inverse scattering methods are still not commonly used in geophysics because of the complexity of the mathematical methods, and because of the relatively stringent data bandwidth requirements.

We detail here one of the algorithms. The two parts to the simulation chain are the forward model and the inversion. The forward model will use standard routines found within the CREWES Matlab toolkit and is used to generate the synthetic seismic data in the form of 2D shot profile and various velocity models. The inversion portion and management of its computational issues is our new contribution.

### BASIC SCATTERING THEORY

In the field of forward scattering(Clayton and Stolt (1981)) the Lippmann-Schwinger equation is crucial for solving acoustic scattering problems, this equation is given by

$$G = G_r + G_r V G, \quad (1)$$

where V is the scattering potential and G is the Green's function operator which is the solution to the linear isotropic acoustic wave equation

$$L P = \left( \frac{\omega^2}{K} + \nabla \cdot \frac{1}{\rho} \nabla \right) P = 0, \quad (2)$$

where

$$L = \left( \frac{\omega^2}{K} + \nabla \cdot \frac{1}{\rho} \nabla \right), \quad (3)$$

and L for the reference medium is

$$L_r = \left( \frac{\omega^2}{K_r} + \nabla \cdot \frac{1}{\rho_r} \nabla \right), \quad (4)$$

so the Green's function is simply the inverse of this operator.

$$G = L^{-1}, \quad (5)$$

and where  $\rho$  and K are the density and bulk modulus respectively. G and  $G_r$  are the Green's function perturbation and the Green's function reference operator (the slowly varying background about which it is perturbed).

This has is only a very brief overview of the essential basis of scattering theory, a more through examination requires a detailed understanding of Partial Differential Equation methods such as Transform methods see Constanada (2010), plus the use of Green's

function operator methods see Duffy (2001). For a thorough mathematical approach to multidimensional inversion the book by Bleistein et al. (2001) is recommended. The application of Green's theorem to many types of problems in geophysics can be found in the review paper by Ramirez et al. (2009). A very thorough review of inverse scattering theory and its application in seismic exploration can be found in Weglein et al (2003).

## **SCIENTIFIC GOALS AND CODE DEVELOPMENT**

This project is in an early stage of implementation and therefore not all code design decisions will be the most optimal.

The code for this modeling/simulation is divided into two parts. The first is the forward modeling code, used to generate the 2D synthetic shot profiles, given a user created velocity model plus a source/receiver configuration. This is done via a centered finite differencing scheme and based on finite difference routines already coded in the CREWES Matlab toolkit. The second portion of the simulation is comprised of inversion code.

### **PART 1: THE FORWARD MODEL**

The creation of the synthetic shot gathers used the finite difference approach rather than any other methods such as raytracing, although the 2D FD method is computationally more expensive, it is also very accurate to an arbitrary order. In this case we have a choice of either using a second or fourth order Laplacian in computing at each node of the model grid.

#### **Creation of an initial velocity model**

The initial velocity model is created using a gui based tool called *AFD\_VELCREATE* created for the CREWES Matlab toolkit. This tool allows the creation of 2D velocity models based upon arbitrary polygonal shapes, the initial model is then properly gridded to the spacing specified by the user. This model is then saved to a file for later input into the finite differencing section of the code.

#### **CREWES Finite Difference Routines**

The velocity model is created twice in this instance, the first is the background velocity model consisting only of the velocity found on the first layer below the surface. This velocity model is then used to generate the synthetic shot profile as if only the surface layer existed and so only the direct wave is present. In the second stage another shot profile is created with the full velocity model as input, the resulting shot profile includes all primary and multiple reflections. The CREWES toolkit routine used in this stage is *AFD\_SHOTREC* which generates arbitrary 2D shot records given an initial velocity model and an initial snapshot time to start with, usually an time zero snapshot with any initial conditions included.

## Wavelet convolution

For some realism a Ricker wavelet can be created by the user and convolved with the shot profiles to create a final more realistic shot profile which is artificially band limited. The user can select the primary frequency and duration of the Ricker wavelet. If no Ricker wavelet is used the profile generated will be that seen if an delta function impulse is used (ie all possible frequencies are included) Yilmaz (2001).

## Generation of a background and model shotpoint gather

The above routine of generating a background snapshot,  $G_r$  and a full snapshot,  $G$  then convolving with a wavelet is repeated at each receiver point along the desired seismic line with the desired receiver spacing. So each receiver will then have two snapshots associated with it a background consisting of only the direct wave plus another snapshot containing the direct wave, primary reflections and multiple reflections.

## THE INVERSION

The inversion method used in this simulation is taken from Clayton and Stolt (1981)

### The Inversion Algorithm for a Constant Background

We will follow the inversion algorithm outlined in Clayton and Stolt (1981) and use their notation as well. The Born approximation of the Lippmann-Schwinger equation is given by the series expansion of the implicit equation

$$G = (I - G_r V)^{-1} G_r, \quad (6)$$

which related the Green's operator  $G$  in the actual medium and the reference operator  $G_r$  and which can be expanded as a series called the Born-Neumann series see Morse and Feshbach (1953) .

$$G = G_r \sum_{i=0}^{\infty} (V G_r)^i. \quad (7)$$

We approximate the total wavefield truncating the expansion. The direct wave in the wavefield is the zeroth order term,  $G_r$  and the primary reflections are approximated by the first order term  $G_r V G$ .

So for the direct wave and the primary reflections we will have

$$G = G_r + G_r V G. \quad (8)$$

### Subtraction of the Direct Wave from the Gathers

The observed wavefield  $D$  is defined as  $D = (G - G_r)S(\omega)$ , and so

$$D = (G - G_r)S(\omega) = (G_r V G)S(\omega). \quad (9)$$

Consequently in order to do a proper inversion of the wavefield, the direct wave  $G_r$  first needs to be subtracted from the seismic profiles. This is done for the current testing purposed by directly subtracting the two wavefields  $G$  and  $G_r$ .

### Deconvolution and Subtraction of the Wavelet

Before the inversion can be done the source wavelet must be subtracted or deconvolved from the transformed wavefield as illustrated below, a small stability factor  $\epsilon$  has been added to the algorithm to prevent any singularities from occurring during this operation.

$$D'(k_m, k_h, k_z) = \frac{-1}{\rho_r} \frac{D(k_m, k_h, \omega)}{S(\omega) + \epsilon}, \quad (10)$$

### Direct Inversion

The first step in the inversion is to Fourier transform the wavefield from source  $x_g$  and receiver  $x_s$  coordinates to source-receiver wavenumbers  $k_g, k_s$ , we will drop the prime notation of the deconvolved wavefield for convenience.

$$D(k_g, k_s, \omega) = \frac{1}{2\pi} \int dx_g \int dx_s e^{-ik_g x_g} D(x_g, x_s, \omega) e^{ik_s x_s}, \quad (11)$$

$$= \int dx' \int dz' G_r^+(k_g, 0|x', z'; \omega) V(x', z'; \omega) G_r^+(x', z'|k_s, 0; \omega) S(\omega), \quad (12)$$

Where  $G_r^+(k_g, 0|x', z'; \omega)$  and  $G_r^+(x', z'|k_s, 0; \omega)$  are Green's operators and have the form given by

$$G_r^+(k_g, 0|x', z'; \omega) = \frac{i\rho_r}{\sqrt{2\pi}} \frac{e^{-i(k_g x' - q_g |z'|)}}{2q_g}, \quad (13)$$

$$G_r^+(x', z'|k_s, 0; \omega) = \frac{i\rho_r}{\sqrt{2\pi}} \frac{e^{i(k_s x' + q_s |z'|)}}{2q_s}, \quad (14)$$

and

$$q_g = \frac{\omega}{\nu_r} \sqrt{1 - \frac{\nu_r^2 k_g^2}{\omega^2}}, \quad (15)$$

$$q_s = \frac{\omega}{\nu_r} \sqrt{1 - \frac{\nu_r^2 k_s^2}{\omega^2}}, \quad (16)$$

So placing the Green's operators into the integral equation we get

$$D(k_g, k_s, \omega) = \frac{-\rho_r^2}{2\pi} \int dx' \int dz' \frac{e^{-i(k_g x' - q_g |z'|)}}{2q_g} V(x', z'; \omega) \frac{e^{i(k_s x' + q_s |z'|)}}{2q_s} S(\omega), \quad (17)$$

Here  $V$  is the scattering potential or the structure we are trying to image, this potential is given by the difference of the two wave operators  $L$  and  $L_r$

$$V = \left( \frac{\omega^2}{K} - \frac{\omega^2}{K_r} \right) + \nabla \cdot \left( \frac{1}{\rho} - \frac{1}{\rho_r} \right) \nabla, \quad (18)$$

Replacing  $K$  and  $\rho$  by dimensionless media operators as follows

$$L = \omega^2 \frac{a_1}{K} + \nabla \cdot \frac{a_2}{\rho} \nabla, \quad (19)$$

where  $a_1, a_2$  are

$$a_1 = \left( \frac{K_r}{K} - 1 \right), a_2 = \left( \frac{\rho_r}{\rho} - 1 \right), \quad (20)$$

Now evaluating the equation relating the data to the scattering potential using  $V$  above

$$D(k_g, k_s, \omega) = \frac{-\rho_r^2}{2\pi} \int dx' \int dz' \frac{e^{-i(k_g x' - q_g |z'|)}}{2q_g} \left[ \left( \frac{\omega^2}{K} - \frac{\omega^2}{K_r} \right) + \nabla \cdot \left( \frac{1}{\rho} - \frac{1}{\rho_r} \right) \nabla \right] \frac{e^{i(k_s x' + q_s |z'|)}}{2q_s} S(\omega), \quad (21)$$

and substituting in  $a_1$  and  $a_2$  then integration by parts we get

$$D(k_g, k_s, \omega) = \frac{-\rho_r^2}{2\pi} \int dx' \int dz' \frac{e^{-i[(k_g - k_s)x' - (q_g + q_s)z']}}{4q_g q_s} \times \left[ \frac{\omega^2}{\nu_r^2} a_1(x', z') + (q_g q_s - k_g k_s) a_2(x', z') \right] S(\omega), \quad (22)$$

Note the absolute value signs around  $z'$  are dropped if we assume  $a_1(x, z)$  and  $a_2(x, z)$  are zero for  $z < 0$ .

The above equation is of the same form as a double Fourier transform in the  $x'$  and  $z'$  variables if we do some rearranging

$$D(k_g, k_s, \omega) = \frac{-\rho_r^2 S(\omega)}{2\pi 4q_g q_s} \int e^{-i(k_g - k_s)x'} \int e^{i(q_g + q_s)z'} \times \left[ \frac{\omega^2}{\nu_r^2} a_1(x', z') + (q_g q_s - k_g k_s) a_2(x', z') \right] dz' dx', \quad (23)$$

the result of the evaluation yields

$$D(k_g, k_s, \omega) = \frac{-\rho_r^2 S(\omega)}{4q_g q_s} \left[ \frac{\omega^2}{\nu_r^2} a_1(k_g - k_s, -q_g - q_s) + (q_g q_s - k_g k_s) a_2(k_g - k_s, -q_g - q_s) \right], \quad (24)$$

### Change of Coordinates to $\omega, q_g, q_s$ space

In order to solve for  $a_1$  and  $a_2$  we will need to change to midpoint/offset coordinates from the source/receiver system.

We have the following definitions the midpoint wavenumber  $k_m = k_g - k_s$ , the half offset wavenumber  $k_h = k_g + k_s$  which in the space domain  $x, z$  correspond to

$$x_m = \frac{x_g + x_s}{2} \quad (25)$$

and

$$x_h = \frac{x_g - x_s}{2} \quad (26)$$

and a new independent variable

$$k_z = -q_g - q_s = -\frac{\omega}{\nu_r} \sqrt{1 - \frac{\nu_r^2 k_g^2}{\omega^2}} - \frac{\omega}{\nu_r} \sqrt{1 - \frac{\nu_r^2 k_s^2}{\omega^2}}, \quad (27)$$

Solving for  $\omega, q_g$  and  $q_s$  we have the expressions

$$\omega(k_m, k_h, k_z) = -\frac{\nu_r k_z}{2} \sqrt{\left(1 + \frac{k_m^2}{k_z^2}\right) \left(1 + \frac{k_h^2}{k_z^2}\right)}, \quad (28)$$

$$q_g(k_m, k_h, k_z) = -\frac{k_z}{2} \left(1 - \frac{k_m k_h}{k_z^2}\right), \quad (29)$$

$$q_s(k_m, k_h, k_z) = -\frac{k_z}{2} \left(1 + \frac{k_m k_h}{k_z^2}\right), \quad (30)$$

Now that we have expressions for  $\omega, q_g, q_s$  the the Direct Fourier transform computed in these coordinates and data can be transformed back after the inversion.

Writing the equation for the wavefield using these new variables substituted according to the definitions above we get

$$D(k_m, k_z, k_h) = \frac{-\rho_r^2 S(\omega)}{4q_g q_s} \left[ \frac{\omega^2}{\nu_r^2} a_1(k_m, k_z) + (q_g q_s - k_g k_s) a_2(k_m, k_z) \right], \quad (31)$$

When transformation variables are substituted in and simplified we obtain the system of equations which need to be inverted.

$$D(k_m, k_z, k_h) = -\rho_r \left[ \sum_{i=1}^2 A_i(k_m, k_h, k_z) a_i(k_m, k_z) \right] S(\omega), \quad (32)$$

where

$$A_1 = (k_m, k_h, k_z) = \frac{1}{4} \frac{(k_z^2 + k_h^2)(k_z^2 + k_m^2)}{k_z^4 - k_m^2 k_h^2}, \quad (33)$$

and

$$A_2 = (k_m, k_h, k_z) = \frac{1}{4} \frac{(k_z^2 - k_h^2)(k_z^2 + k_m^2)}{k_z^4 - k_m^2 k_h^2}, \quad (34)$$

After the deconvolution stage we are left with

$$D'(k_m, k_z, k_h) = \left[ \sum_{i=1}^2 A_i(k_m, k_h, k_z) a_i(k_m, k_z) \right], \quad (35)$$

of which we need to determine the  $a_i(k_m, k_z)$  through perhaps a least squares method.

### Issues in the practical implementation of the inversion algorithm

The deconvolved shot records are now ready for the inversion stage. The basic routine is as follows

1. First loop over a set of grid points in  $k_m, k_z$  space with  $k_h$  set to a fixed value, usually zero.
2. Outer loop ranging over  $k_z$ : For each  $k_z$  from  $k_z$  : Start to  $k_z$  : End
3. Inner loop ranging over  $k_m$ : For each  $k_m$  from  $k_m$  : Start to  $k_m$  : End
4. transform the data into  $(k_m, k_z)$  via the transformation equations for  $(\omega, q_g, q_s)$  given in equations 28, 29 and 30

We need to calculate the Fourier kernels at each grid point

$$\text{kernel } \omega = \exp(-2\pi i * \omega(k_m, k_h, k_z) * t), \quad (36)$$

$$\text{kernel } k_g = \exp(-2\pi i * k_g(k_m, k_h, k_z) * x_{gcenter}), \quad (37)$$

$$\text{kernel } k_s = \exp(-2\pi i * k_s(k_m, k_h, k_z) * x_{scenter}), \quad (38)$$

for each source point in the line we multiply(Fourier transform) that particular shot-gather by the Fourier kernel as follows:

Compute the Fourier transforms over  $(t, x_g, x_s)$  which is a series of multiplications in the wavenumber domain, we will need to perform three Fourier transforms in all. Ranging over the line of sources: For each shotgather in the line from the start to the end of the line, transform first over  $\omega$  then secondly over  $k_g$ .

$$D(k_g, k_s, \omega) = \text{kernel } k_g \times \left[ D(x_g, x_s, t | \text{shotpoint}(i))^T \times (\text{kernel } \omega)^T \right], \quad (39)$$

then compute the final  $k_z$  vector for a fixed  $k_z$  over a range of  $k_m$ .

$$D(k_z) = D(k_g, k_s, \omega) \times (\text{kernel } k_s)^T, \quad (40)$$

In summary we compute,

$$D'(k_z(k_m, k_h)) = \left[ \text{kernel } k_g \times (D(x_g, x_s, t; \text{shotpoint}(i))^T \times (\text{kernel } \omega)^T) \right] * (\text{kernel } k_s)^T, \quad (41)$$

or

$$D'(k_z(k_m, k_h)) = \left[ (e^{-2\pi i * k_g(k_m, k_h, k_z) * x_{gctr}}) \times D(x_g, x_s, t; \text{shotprofile}(i))^T * (e^{-2\pi i * \omega(k_m, k_h, k_z) * t})^T \right] \times (e^{-2\pi i * k_s(k_m, k_h, k_z) * x_{sctr}})^T, \quad (42)$$

This creates an array of  $k_z$  values which form a column vector with the number of elements equal to  $k_m$  points, these series of column vectors represent varying  $k_z$  values so combining all the columns into a matrix will create the an image of  $k_z$  by  $k_m$  elements, we then take the 2D FFT of this  $[k_z, k_m]$  array to obtain the proper inversion image in x and z space.

We need to keep in mind in this case we are performing direct Fourier transforms or DFTs from point to point on a grid, we chose a fixed range  $[k_z, k_m]$  grid and computed the coordinate transforms via equations 28,29,30 into  $(\omega, q_g, q_s)$  space. But the equations which do the mapping are not linear at all, so the spacing between each given  $(k_z, k_m)$  node does not map to a regularly spaced  $(\omega, q_g, q_s)$  grid but a highly non linear one.

Because of this fact, choosing to do a DFT is computationally slower than doing a fast Fourier transform(FFT) from one grid to another, the advantage is that we are much more accurate as we don't need to interpolate points in  $(\omega, q_g, q_s)$  space to create a regularly spaced grid there, the disadvantage is the sacrifice in speed the FFT brings to the problem. Note we do use a fast inverse Fourier transform(IFT) compute the inversion image from the  $k_z, k_m$  grid to x,z space since both are regularly spaced one-to-one grids.

## SYNTHETIC EXAMPLES

We have chosen to test our inversion process using three cases. A four layer model with constant horizontal velocities in each layer but different from layer to layer. A "shallow"

body containing low velocity material intruding into a 4 layer model background which contains a concave top surface and a convex bottom surface. Finally, a case where again there is an intrusion into a background four layer model but this time the body has a strongly concave upper surface and a convex lower surface containing higher velocity material than the surroundings.

For these experiments we have fixed the model parameters at a x line length of 2500m and a depth of 1000m (corresponding to a time of approximately 0.8 sec), we then choose a source/receiver spacing of 10m and a sampling time of 4ms. For the forward differencing calculations the time step is 0.5ms between frames and a computation grid of 10m in the x direction and 5m in the z direction. A bandlimited source wavelet was also added which in this case is a Ricker wavelet with a user specifiable frequency and duration, we used 30Hz and 0.1 seconds.

For each case the initial velocity map used as input into the CREWES forward differencing routines displayed, followed by a snapshot at one particular source point comprising the gather of the receivers for that source point. A deconvolution was then done on all the shot profiles and a single one is displayed, usually at the same source point, the displayed image is also missing the direct wave as this was subtracted prior to the deconvolution.

The computation of the  $k_z, k_m$  grid needed to sample enough of the k-space grid to give the proper resolution and details. Initially we found that sampling only the points in quadrant 1 ( $+k_z, +k_m$ ) produced inversions which were incomplete, only reflectors with a positive slope were imaged and the structures with a negative spatial slope were absent. When we sampled k-space quadrant 4 ( $+k_z, -k_m \rightarrow 0$ ) plus quadrant one ( $+k_z, 0 \rightarrow +k_m$ ) we were able to obtain a complete and structurally correct inversion. The inversion was then computed and two more images were produced, an image in  $k_z, k_m$  space prior to the IFT and then the final inversion image with the IFT performed on the  $k_z, k_m$  grid.

The shotpoint images were scaled using mean value and not max value scaling to bring out the details of each of the models and results. Max value scaling produced images with a bright spot at the top, where the wave amplitudes from the shot is the greatest and the rest of the image was too faint to clearly see the details due to geometric spreading.

### **Four layer horizontal model**

This physically simple model demonstrates the power and accuracy of the inversion routine, in figure 3 and figure 4 we get the expected responses from the forward differencing model. Hyperbolic features corresponding to the model reflectors and in the deconvolved case as in all cases we've subtracted the direct wave. We do get some high frequency "wakes" following each of the hyperbolic returns plus reflections from the sides of the aperture. Note the z axis is labeled in time, this is because of the output of the particular CREWES plotting routine used and in which there wasn't time to change over to a depth labeled axis.

In Figure 5 we can see a very simple one dimensional column, this is because there is only the horizontal reflectors which are flat and so no variance in relative angle the source

and no "slope" their a straight vertical column is expected. Figure 6 shows the resulting inversion, again we have some wakes and aperture artifacts on the sides. But we do get the expected number of layers with reflector 1 at the model depth expected. The difference is in the depth of the second and subsequent layers. Reflector 2 and 3 are shallower then expected because there is a difference in layer velocities which are not accounted for in the inversion algorithm below the first reflector. This is due to the number of terms in the Born approximation that we take. This effect will be apparent across all the models we choose to use.

### **The Shallow low velocity model**

The shallow, low velocity model was created to see if the inversion properly placed the deep reflectors when encountering a low velocity layer. In this case we have a biconvex lens As can be seen from Figures 8 and 9 there is a lot of detail in the lower parts of the shot profile. This is complicated by the high frequency wakes generated by the structures so it's very difficult to tell what is a true reflector and what is noise.

In Figure 10 we can see how the signal is distributed in k-space, there is a broad area of signal in a cone with some possible aliasing. Finally in Figure 11 the inversion image looks fairly realistic, compared to the velocity model the upper and lower reflectors have the correct shape and form. Again the lower convex part of the intrusion is not located in exactly the correct depths due to the velocity difference not being accommodated by the inversion algorithm. Note the deformation of the lowest reflector layer at  $z=850\text{m}$  depth in the model and how it distorts from a horizontal reflector in the model into a concave shape, due to the distortion in travel times introduced by the low velocity found in the intrusion.

### **The Anticline velocity model**

The Anticline velocity model shown in figure 12 also has a low velocity center but has a concave upper surface and a convex lower surface which should create significant distortion. The sides of the upper surface have a greater slope towards the ends while the lower surface has a fairly consistent and shallow angle.

Unlike the shallow biconvex lens model the anticline model seems to have less noise and a cleaner profile as seen in figures 13, the Ricker convolved data and the deconvolved shotgather in figure 14, figure 15 seems to have a cleaner look as well with less apparent spread in the signal. Of course the inversion image in figure 16 shows that the structure was reproduced fairly accurately, the steeper side of the upper surface seem to drop in amplitude as a result of the large angles with respect to the placement of the source and only shows up weakly in the plot. Even a clear velocity push down is see at the lower convex surface on the body where the apparently horizontal layer looks distorted and the lower velocity through the intrusion produced a longer travel time.

## **CONCLUSION**

Inverse scattering techniques provide direct means of determining multidimensional variations in multiple acoustic or elastic parameters. Clayton and Stolt (1981) presented

one of the earliest, with clarity, and a facility for extension to more complex models, that makes it a foundation for any ultimate modern application. We have completed early code development and synthetic testing, restricting ourselves to scalar acoustic problems. We have confirmed that correct depths and structures are recovered.

Even with the relatively straightforward algorithm for a constant background, we are able to image the models to a fairly high degree of accuracy. Of course our simulations have not taken into account real world effects such as multiples and anisotropic and anelastic media which are variable background effects. We verify that the amplitudes of the reflections found in these results are true amplitudes. Also material parameters such as bulk modulus, variable density be built into the models to test the accuracy of the inversions in producing the correct, physically realistic answers.

Much more remains to be done in regards to further numerical investigations of multi-parameter inverse scattering and the inversion algorithms predicted by this approach.

## REFERENCES

- Aki, K., and P. G. Richards, 2002, *Quantitative Seismology* (2nd ed.): University Science Books
- Bleistein, N., J. Cohen and J. Stockwell, 2001, *Mathematics of Multidimensional Seismic Imaging, Migration and Inversion*: Springer-Verlag.
- Claerbout, J. F., 1968, Synthesis of a layered medium from its acoustic transmission response: *Geophysics*, 33, 264-269.
- Clayton, A.W. and Stolt, R.H., 1981, A Born-WKBJ inversion method for acoustic reflection data, *Geophysics*, 46, 1559-1567.
- Constanada, C., 2010, *Solution Techniques for Elementary Partial Differential Equations*: Chapman and Hall/CRC
- Duffy, D.G., 2001, *Green's Functions with Applications*: Chapman and Hall/CRC
- Innanen, K., 2010, A theoretical note on scattering and diffraction of radar waves from a seismic disturbance propagating in the near-surface, *CREWES Research Reports*, 22
- Morse, P., and H. Feshbach, 1953, *Methods of Theoretical Physics, Part 1*. McGraw-Hill.
- Ramirez, A.C., and A. Wieglein, 2009, Green's theorem as a comprehensive framework for data reconstruction, regularization, wavefield separation, seismic interferometry, and wavelet estimation: *A tutorial: Geophysics*, 74, W35-W62
- Arthur B Wieglein, Fernanda V Araújo, Paulo M Carvalho, Robert H Stolt, Kenneth H Matson, Richard T Coates, Dennis Corrigan, Douglas J Foster, Simon A Shaw1, and Haiyan Zhang, 2003, Inverse scattering series and seismic exploration, *Inverse Problems*, 19, R27-R83
- Yilmaz, O., 2001, *Seismic Data Analysis: Processing, Inversion and Interpretation of Seismic Data*, 2nd edition: SEG Publishing

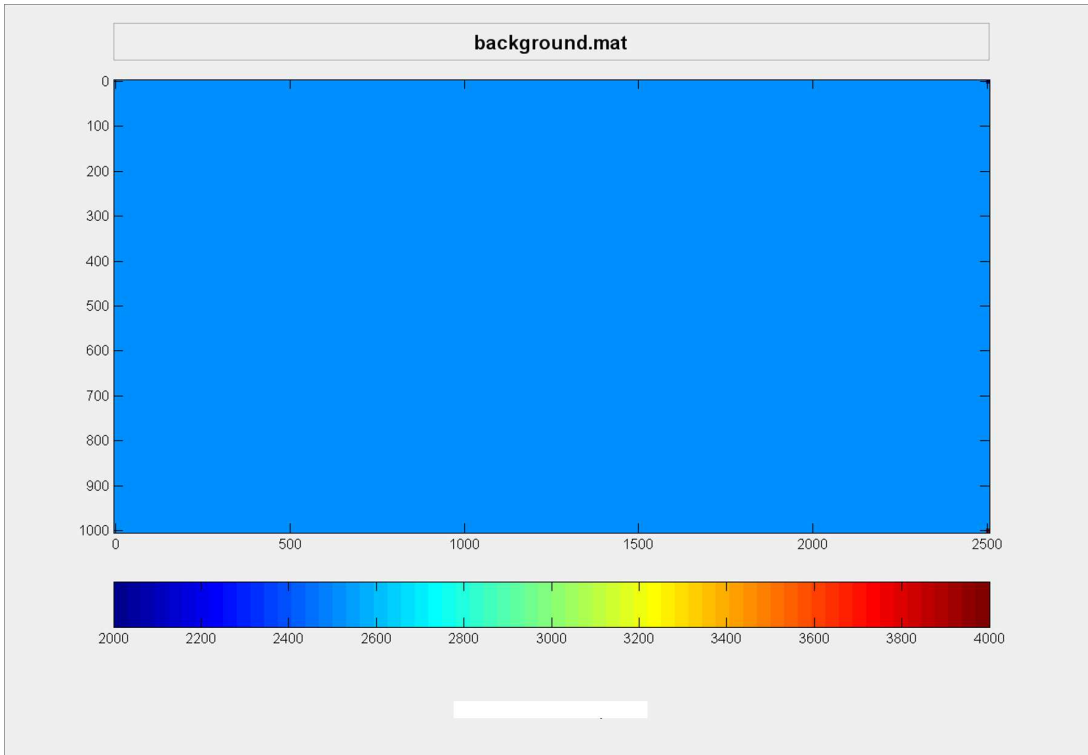


FIG. 1: Background velocity model

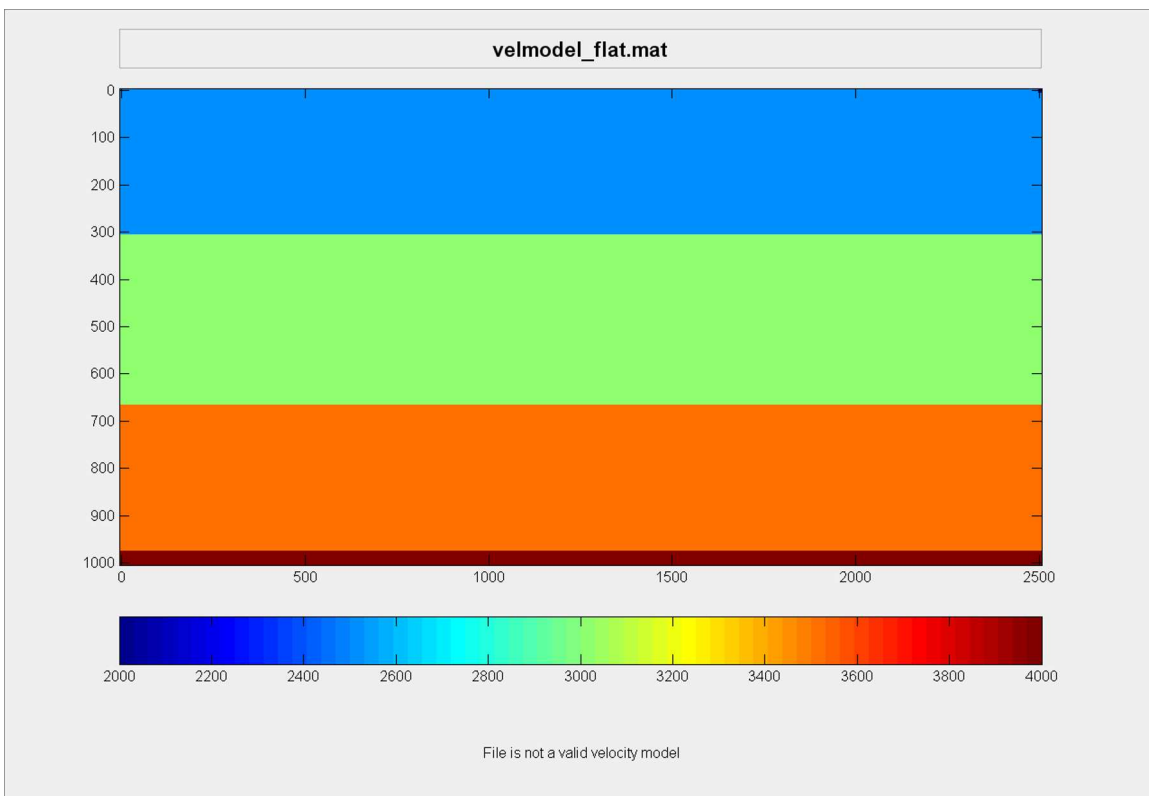


FIG. 2: 4 Layer flat velocity model

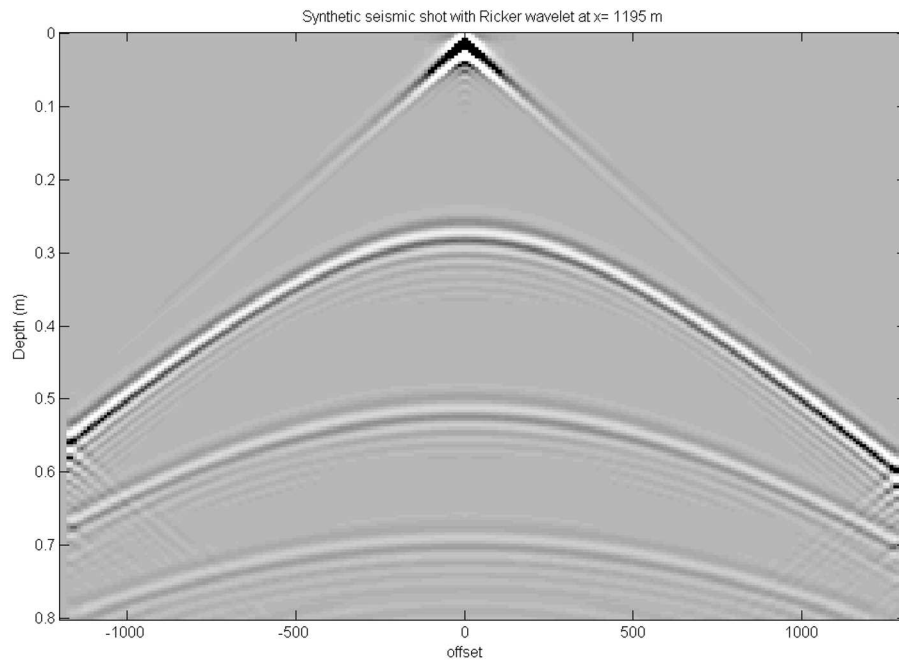


FIG. 3: 4 Layer flat velocity model, synthetic data with 30 Hz ricker wavelet, x=1195m

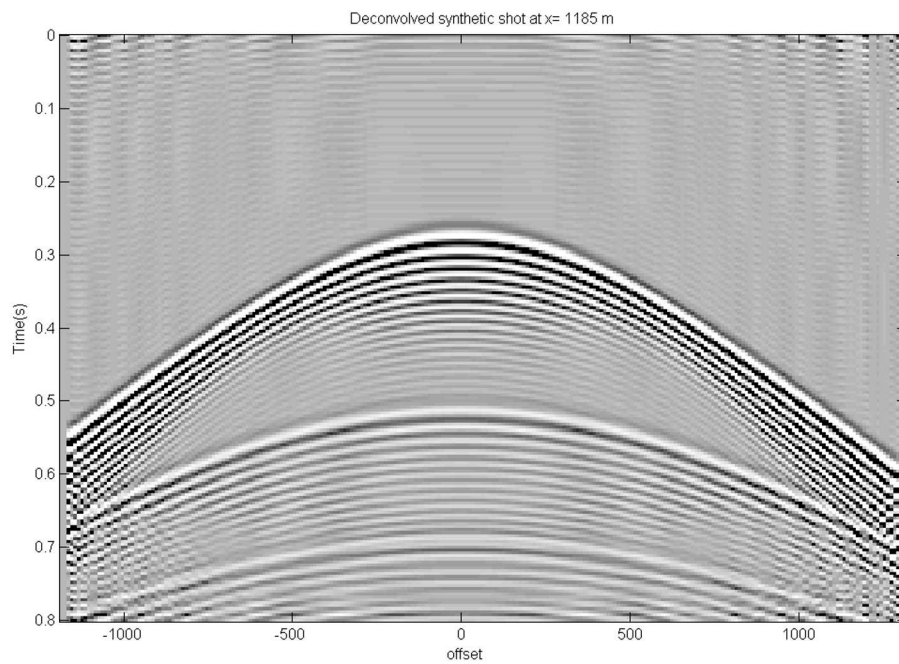


FIG. 4: 4 Layer flat velocity model, deconvolved synthetic data, x=1195m

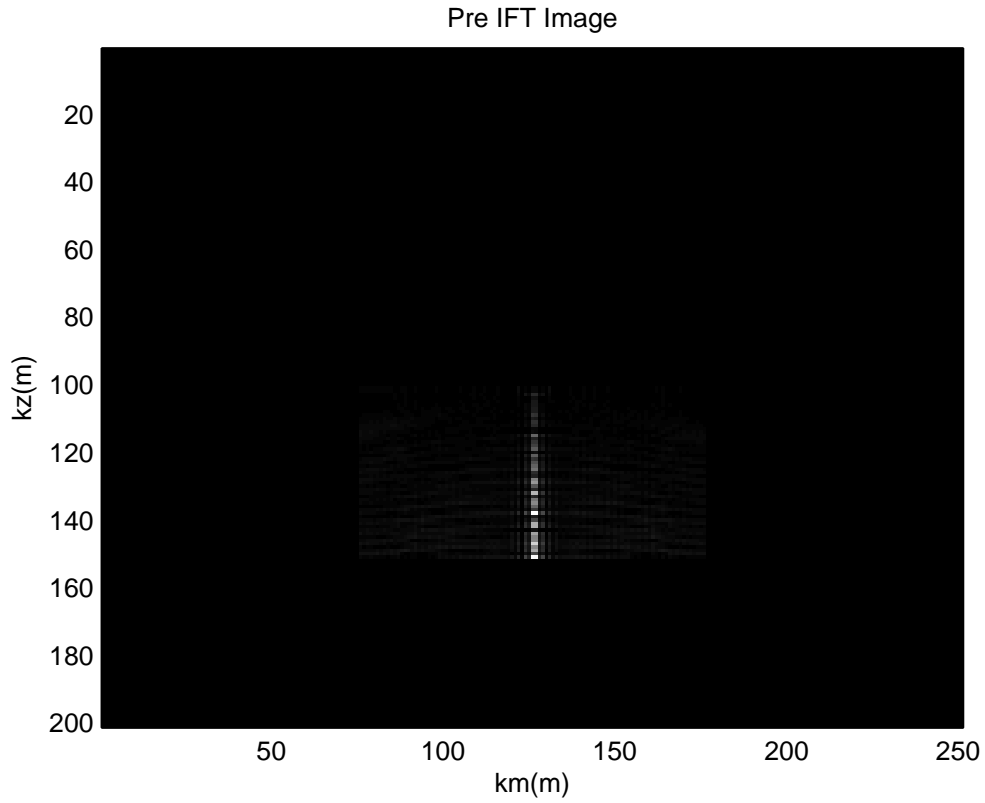


FIG. 5: 4 Layer flat model  $k_z k_h$  plot

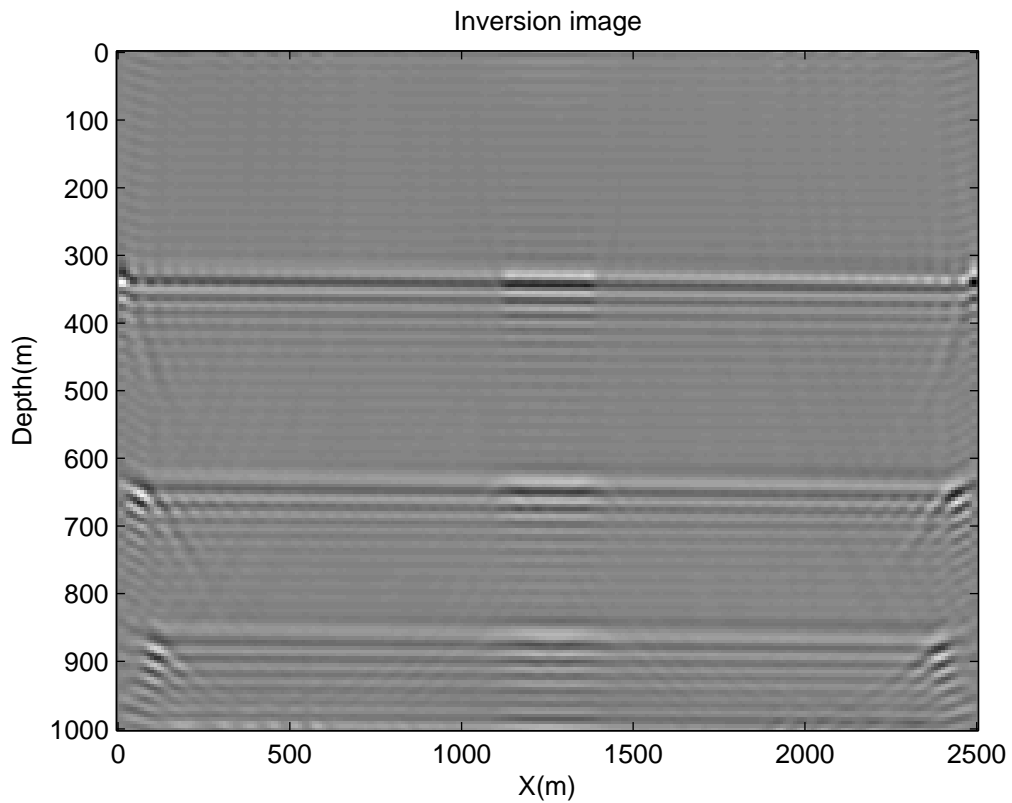


FIG. 6: 4 Layer flat model, inversion result

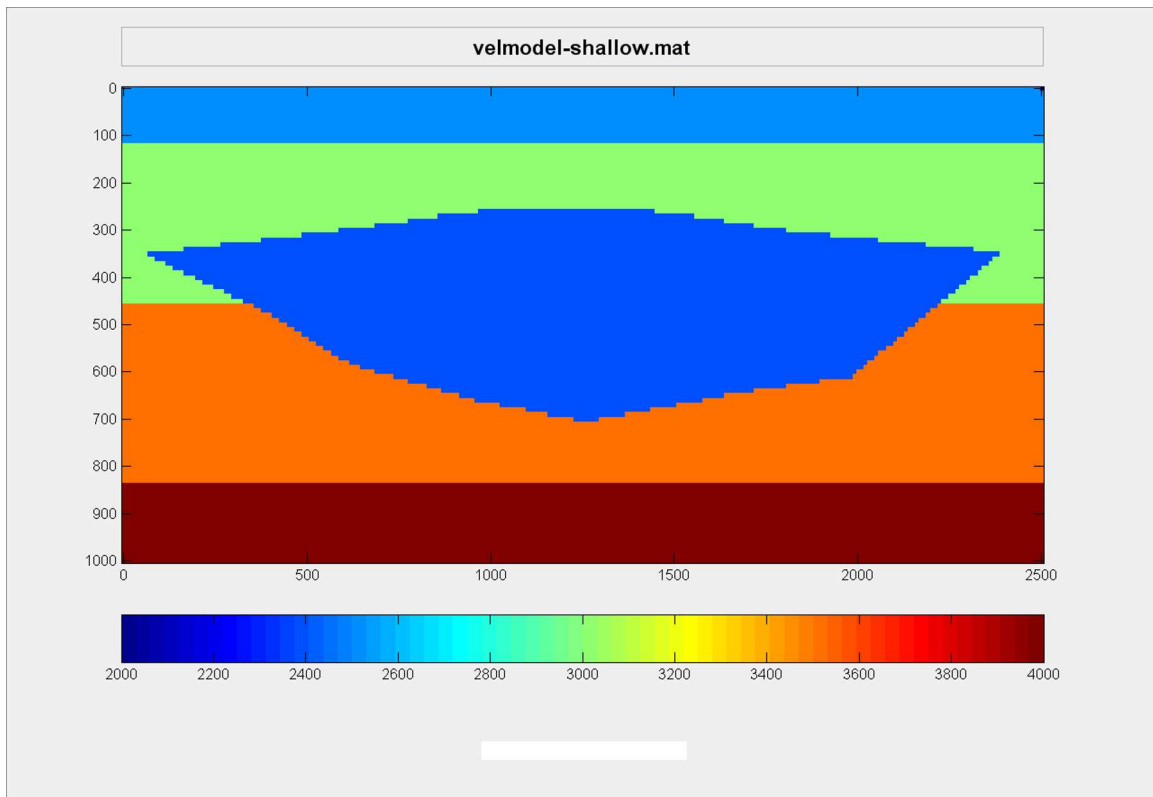


FIG. 7: Shallow dip velocity model

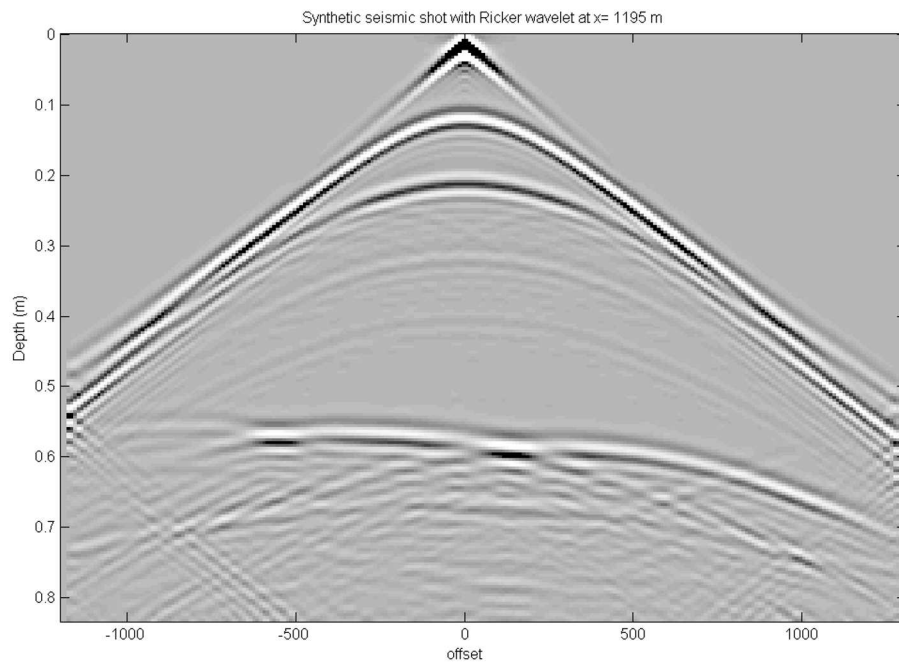


FIG. 8: Shallow dip velocity model, synthetic data with 30 Hz ricker wavelet, x=1195m

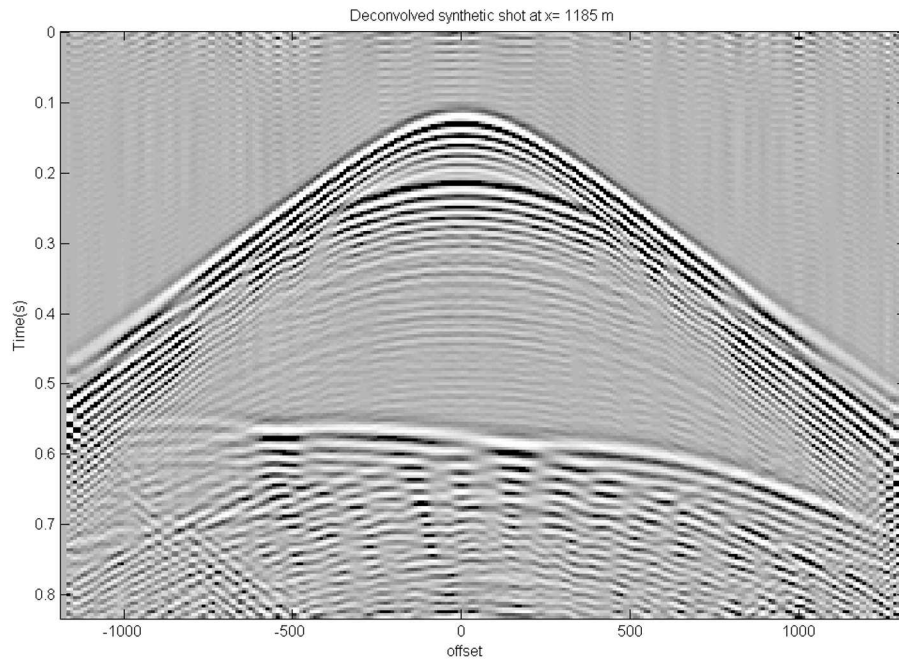


FIG. 9: Shallow dip velocity model deconvolved synthetic data ,x=1195m

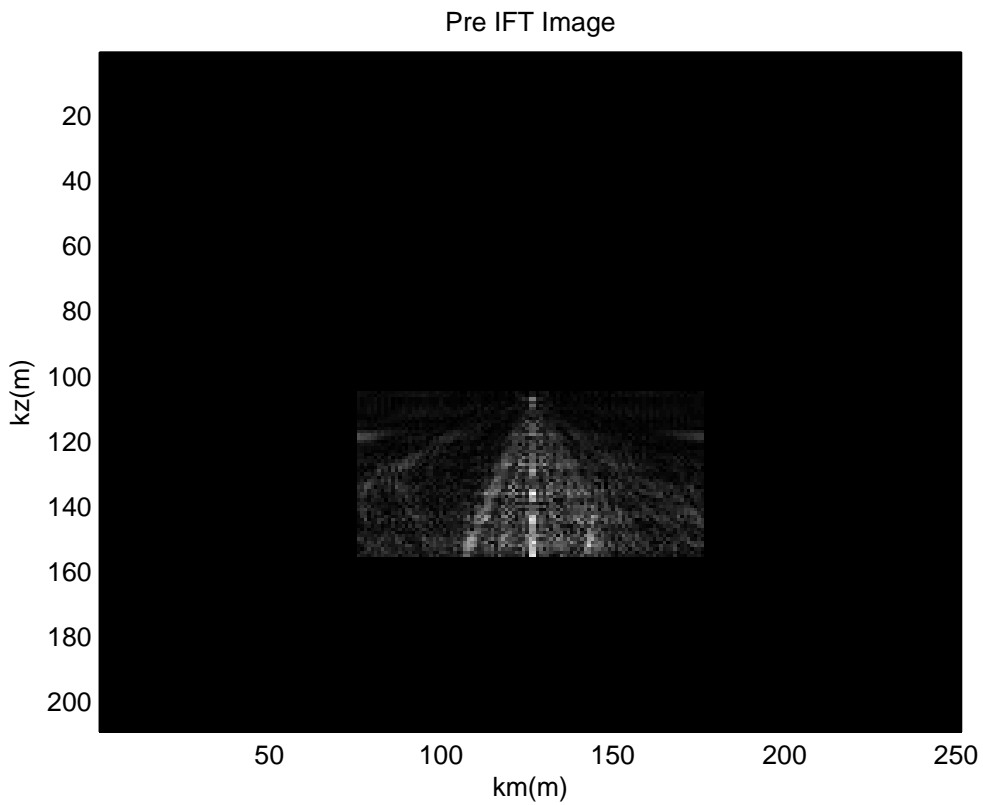


FIG. 10: Shallow dip velocity model,  $k_z$   $k_h$  plot

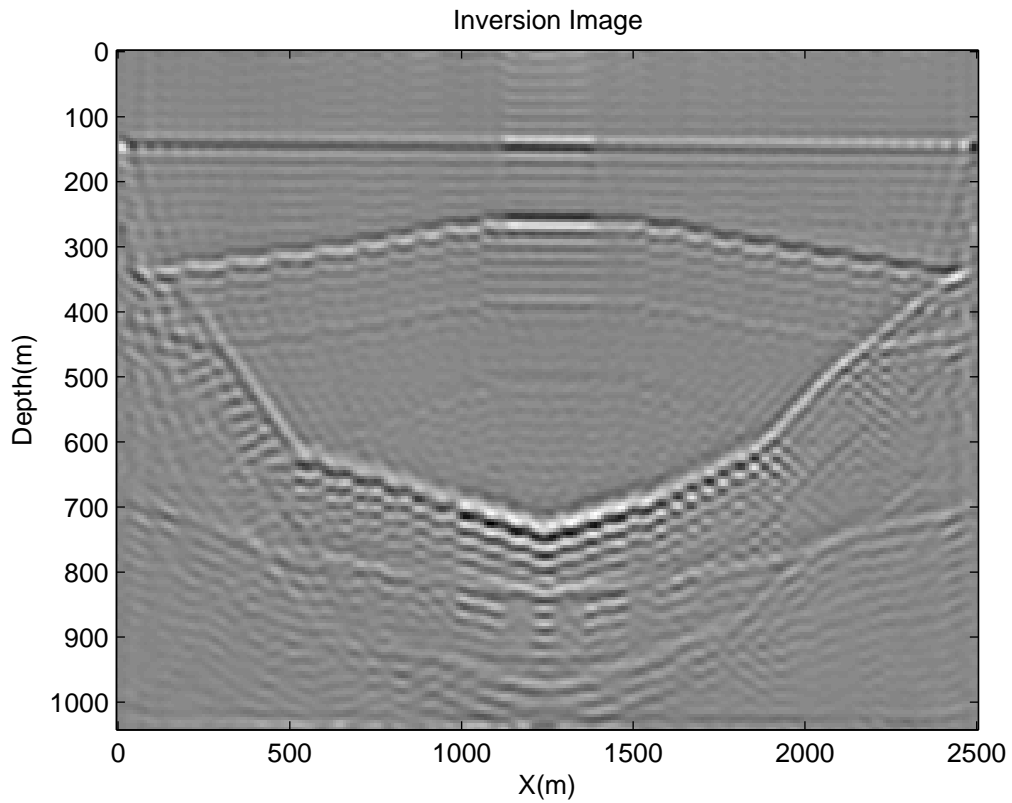


FIG. 11: Shallow dip velocity model, inversion result

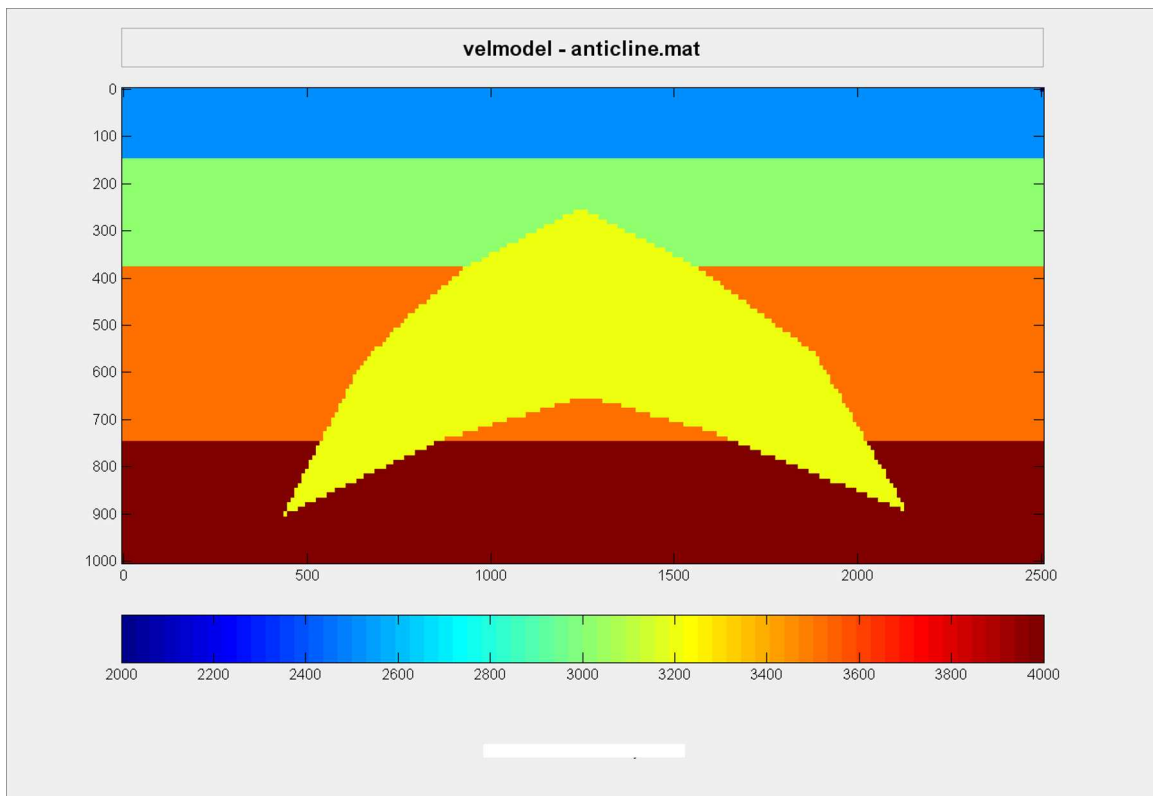


FIG. 12: Anticline velocity model

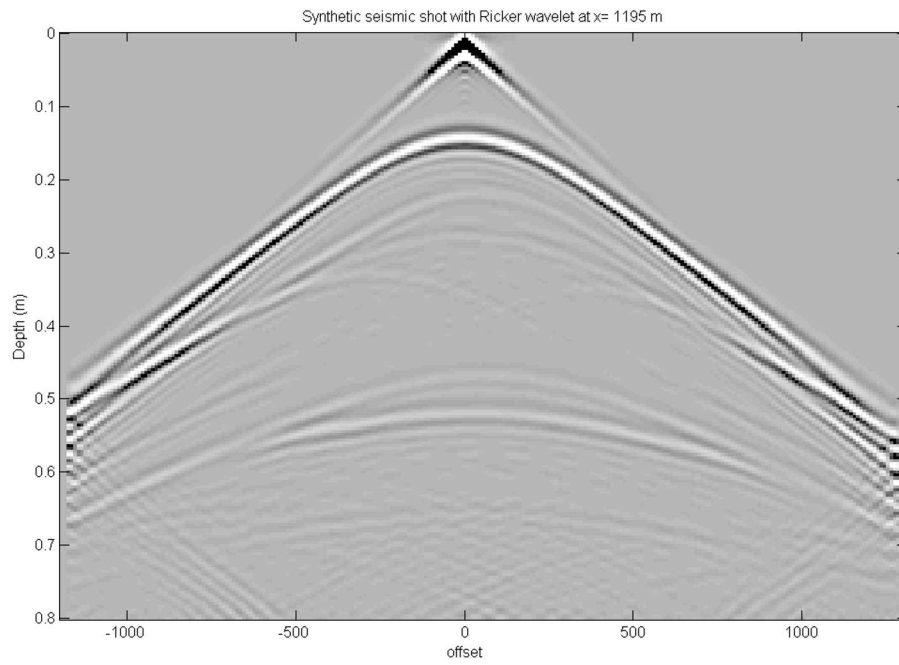


FIG. 13: Anticline synthetic shot profile with 30 Hz ricker wavelet, x=1195m

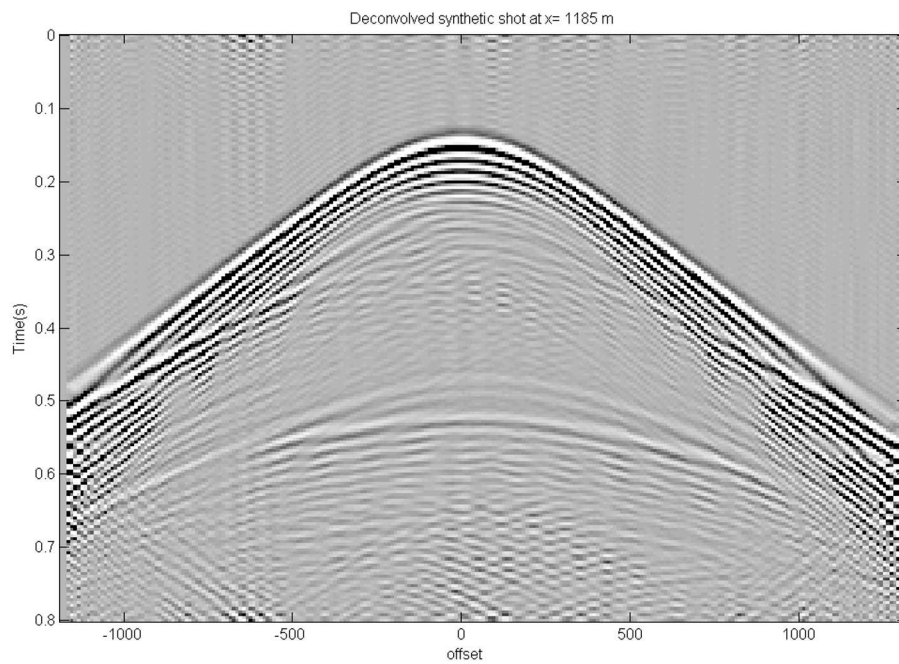


FIG. 14: Anticline deconvolved synthetic shot profile, x=1195m

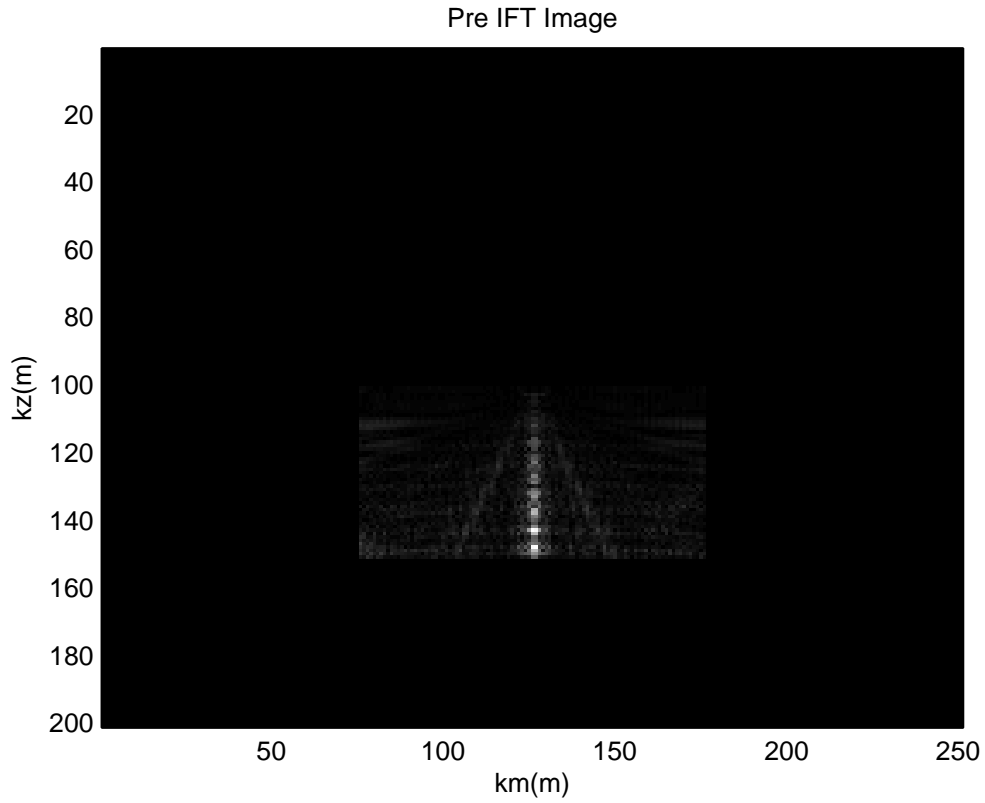


FIG. 15: Anticline velocity model,  $k_z$   $k_h$  Plot

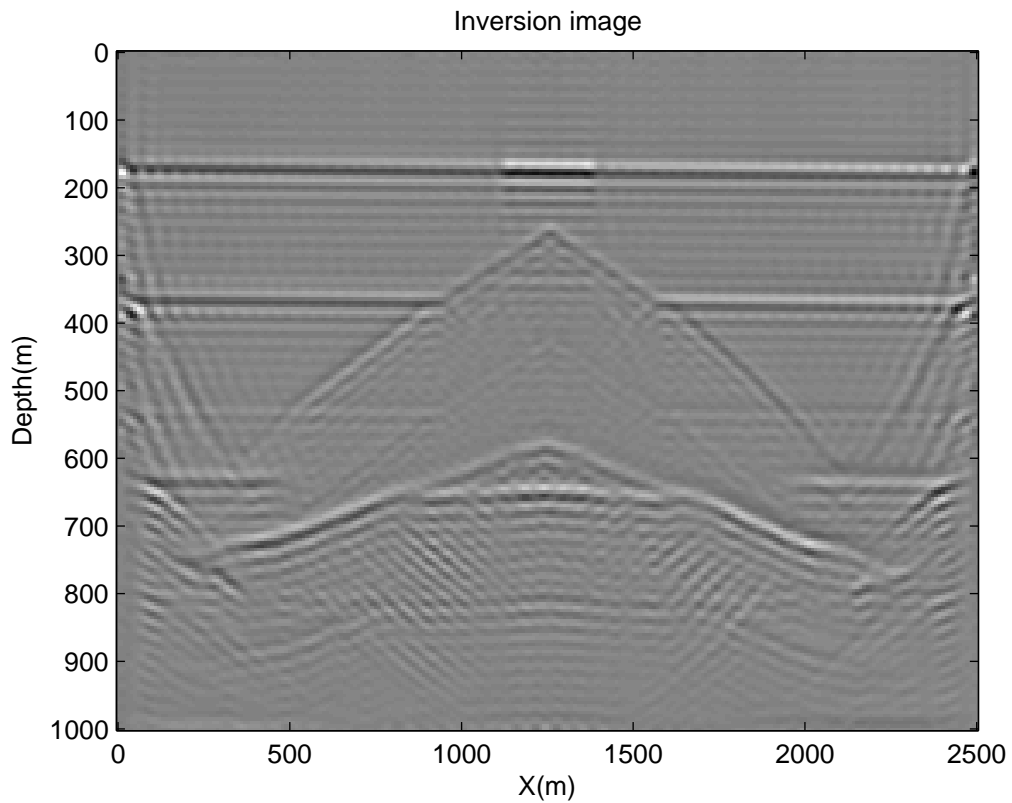


FIG. 16: Anticline velocity model, inversion result